ChemPubSoc Europe

DOI: 10.1002/chem.201700399

CHEMISTRY A European Journal Full Paper

Magnetic Properties

Role of the Diamagnetic Zinc(II) Ion in Determining the Electronic Structure of Lanthanide Single-Ion Magnets

Apoorva Upadhyay,[a] Chinmoy Das,[a] Shefali Vaidya,[a] Saurabh Kumar Singh,[a] Tulika Gupta,[a] Ranajit Mondol,[a] Stuart K. Langley,[b] Keith S. Murray,[c] Gopalan Rajaraman,*[a] and Maheswaran Shanmugam*[a]

Abstract: Four complexes containing Dy^{III} and Pr^{III} ions and their Ln^{III}–Zn^{II} analogs have been synthesized in order to study the influence that a diamagnetic Zn^{II} ion has on the electronic structure and hence, the magnetic properties of the Dy^{III} and Pr^{III} single ions. Single-crystal X-ray diffraction revealed the molecular structures as $[Dy^{III}(HL)_2(NO_3)_3]$ (**1**), $[Pr^{III}(HL)_2(NO_3)_3]$ (**2**), $[Zn^{II}Dy^{III}(L)_2(CH_3CO_2)(NO_3)_2]$ (**3**) and $[Zn^{II}_2Pr^{III}(L)_2(CH_3CO_2)_4(NO_3)]$ (**4**) (where HL = 2-methoxy-6-[(*E*)-phenyliminomethyl]phenol). The dc and ac magnetic data were collected for all four complexes. Compounds **1** and **3** display frequency dependent out-of-phase susceptibility signals (χ_M''), which is a characteristic signature for a single-molecule magnet (SMM). Although **1** and **3** are chemically similar, a fivefold increase in the anisotropic barrier (U_{eff}) is observed experimentally for **3** (83 cm^{-1}), compared to **1** (16 cm^{-1}). To rationalize the larger anisotropic barrier (**1** vs. **3**), detailed ab initio calculations were performed. Although the ground state Kramer's doublet in both **1** and **3** are axial in nature ($g_{zz} = 19.443$ for **1** and 18.82 for **3**), a significant difference in the energy gap (U_{eff}) between the ground and first excited Kramer's doublet is calculated. This energy gap is governed by the electrostatic repulsion between the Dy^{III} ion and the additional charge density found for the phenoxo bridging ligand in **3**. This extra charge density was found to be a consequence of the presence of the diamagnetic Zn^{II} ion present in the complex. To explore the influence of diamagnetic ions on the magnetic properties further, previously reported and structurally related Zn–Dy^{III} complexes were analyzed. These structurally analogous complexes unambiguously suggest that the electrostatic repulsion is found to be maximal when the Zn-O-Dy-O dihedral angle is small, which is an ideal condition to maximize the anisotropic barrier in Dy^{III} complexes.

Introduction

The presence of unquenched orbital angular momentum for the majority of trivalent lanthanide ions makes them attractive candidates towards developing new molecular magnetic materials.[1] Exploiting the large intrinsic orbital angular momentum of Ln^{3+} ions allowed for the observation in 2003 of slow relaxation of the magnetization in a Tb^{III} bispthalocyanine sandwich complex; the first lanthanide complex to display such behavior.[2] This property, which is of purely molecular origin, led to the term single-molecule magnet (SMM). If the property originates from a single metal ion, then the term single-ion magnet (SIM) is preferably used. SMMs or SIMS offer a host of potential applications such as high density data storage, as molecular qubits, and as components in spintronic devices.[3] In addition other novel magnetic phenomena such as single-molecule toroidal behavior have been detailed.[4] Numerous lanthanide-based coordination complexes have subsequently flooded the literature,[5] with examples revealing record high anisotropy barriers (U_{eff}), the energy required to flip the orientation of the magnetization vector, with values as large as 1261 cm^{-1}.[6] Although the magnitude of the anisotropy barrier is significantly larger than the average thermal energy at room temperature, in many SMM complexes the blocking temperature (T_B), given as a magnetization relaxation time of 100 s, lies at extremely low temperatures, usually < 2 K, due to quantum tunneling of the magnetization (QTM). At the present time there is no straightforward route towards tackling the problem of this quantum behavior; however, one method of subduing QTM can be achieved by enhancing the exchange interaction between lanthanide ions. This was elegantly shown by Long and co-workers in radical bridged dinuclear lanthanide complexes.[7] Upon arresting the fast QTM, significant gains in the blocking temperature were observed; $T_B = 14$ K for a N_2^{3-} radi-

[a] A. Upadhyay, C. Das, S. Vaidya, S. K. Singh, T. Gupta, R. Mondol, Prof. G. Rajaraman, Prof. M. Shanmugam
Department of Chemistry, Indian Institute of Technology Bombay
Powai, Mumbai, Maharashtra, 400076 (India)
E-mail: rajaraman@chem.iitb.ac.in
eswar@chem.iitb.ac.in

[b] Dr. S. K. Langley
School of Science and the Environment, Division of Chemistry
Manchester Metropolitan University, Manchester M15 6BH (UK)

[c] Prof. K. S. Murray
School of Chemistry, Monash University
Clayton 3800, Victoria (Australia)

Supporting information and the ORCID identification numbers for the authors of this article can be found under http://dx.doi.org/10.1002/chem.201700399.

cal bridged Tb^{III}_2 complex.[7a] Enhancing the magnetic exchange interaction of Ln^{III} ions can also be achieved using transition metal ions. Complexes such as $\{Cr^{III}_2Dy^{III}_2\}$ and $\{Ni^{II}_2Dy^{III}_2\}$, reported by us, have shown a significant reduction in QTM due to the non-negligible magnetic exchange interactions between Dy^{III} and transition metal ions.[8] Although the above-mentioned statement holds true, a suitable ligand field around the lanthanide ions plays a substantial role in opening or arresting the under barrier relaxation (QTM) mechanism.[9] Undeniably a combination of strong magnetic exchange along with a suitable ligand field around the lanthanide ion(s) will drastically enhance the blocking temperature of lanthanide complexes.

It has been shown that the orientation of the g_{zz} axis in anisotropic lanthanide ion complexes is governed by the electrostatic charges of the ligands rather than the geometry.[1b,9,10] An appropriate ligand design and coordination environment based on the nature of the ion is therefore required. For example, for a 4f ion with a prolate electron density distribution, an equatorial ligand field is preferred; whereas, if an oblate ion is used, an axial ligand field is preferred. These conditions are necessary to stabilize the Ising magnetic anisotropy in those complexes.[9] Such an approach appears to be a promising route for stabilizing SMMs, with a mononuclear dysprosium complex revealing magnetic hysteresis up to 30 K (sweep rate 20 mTs^{-1}) using this strategy.[5a]

It is not a trivial exercise to control the exchange interaction between 3d and 4f ions, with the majority of 3d–4f metal complexes exhibiting weak exchange interactions, leading to fast magnetic relaxation. Due to these observations, our focus has shifted towards modifying and controlling the electrostatic charge of the ligand field that governs the orientation of the g_{zz} axis, as this may be easier to modify and optimize for a particular system. A means to modulate the electrostatic charge around the trivalent Ln ion has been developed by incorporating the diamagnetic Zn^{II} ion into various complexes.[11] The factors that influence the magnetization relaxation dynamics using this approach are reported from the study of four complexes of molecular formulae: $[Ln^{III}(HL)_2(NO_3)_3]$ where Ln^{III} = Dy (**1**) or Pr (**2**), $[Zn^{II}Dy^{III}(L)_2(CH_3CO_2)(NO_3)_2]$ (**3**) and $[Zn^{II}_2Pr^{III}(L)_2(CH_3CO_2)_4NO_3]$ (**4**), where HL = 2-methoxy-6-[(*E*) phenyliminomethyl]phenol.

Results and Discussion

To probe the effect of incorporating a diamagnetic ion such as Zn^{II} on the electronic structure and therefore the magnetic properties of lanthanide-based single-ion magnets (SIMs), a series of homometallic and heterometallic complexes were synthesized. The reaction of the neutral Schiff base ligand 2-methoxy-6-[(*E*)-phenyliminomethyl] phenol (HL) with $Ln(NO_3)_3{\cdot}xH_2O$ (where Ln = Dy or Pr) in ethanol or methanol yielded orange crystals that were suitable for X-ray diffraction study (Scheme 1).

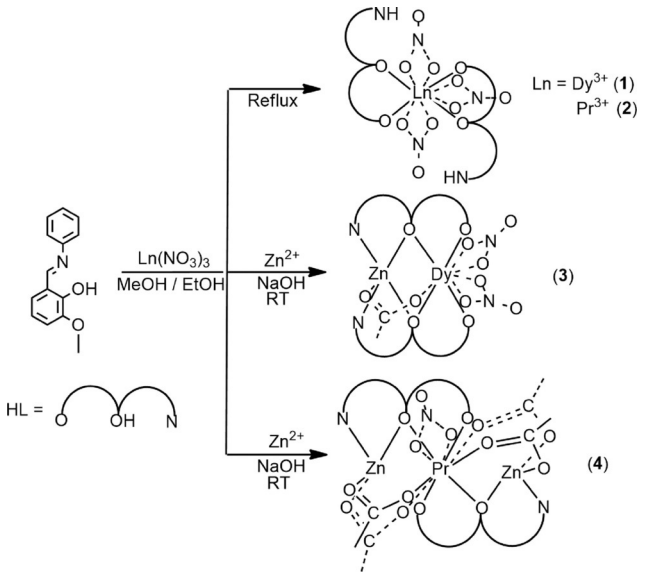

Scheme 1. General synthetic method followed for the isolation of complexes **1**–**4**.

Structural description

Single-crystal X-ray diffraction studies revealed the molecular formulae as $[Dy(HL)_2(NO_3)_3]$ (**1**) and $[Pr(HL)_2(NO_3)_3]$ (**2**) following the top reaction in Scheme 1. Using the deprotonated ligand (L) and $Dy(NO_3)_3{\cdot}xH_2O$ in the presence of zinc acetate $[ZnDy(L)_2(CH_3CO_2)(NO_3)_2]$ was obtained (**3**) (see middle panel in Scheme 1); when $Pr(NO_3)_3{\cdot}xH_2O$ was used, $[Zn_2Pr(L)_2(CH_3COO)_4(NO_3)]$ (**4**) was obtained (Scheme 1, bottom panel).

The crystal structures of all four complexes are shown in Figure 1. Complexes **1** and **2** crystallize in the orthorhombic space groups, *Aba*2 and *Pbca*, respectively. Complexes **3** and **4** crystallize in triclinic ($P\bar{1}$) and monoclinic (*C*2/*c*) crystal systems, respectively (Table 1).

The homometallic mononuclear complexes **1** and **2** reveal that the lanthanide ion is 10-coordinate, with a bicapped distorted square *anti*-prism geometry (Figures 1 D–F). The geometries were confirmed by the Continuous Shape Measurement (CShM) software.[12] The three chelating nitrate ions in **1** and **2** account for six out of the ten coordination sites, neutralizing the trivalent cationic charge on the lanthanide ion. The remaining four coordination sites are completed by the two neutral Schiff base ligands; however, the proton bound to the phenolic oxygen of the free ligands has migrated to the imine nitrogen atom upon coordination with the lanthanide ion.[13]

The two HL ligands bound to the metal ion therefore exist as a zwitterion, which has been unambiguously confirmed by NMR spectroscopy.[10a,11,14] The lanthanide ion for both **1** and **2** are exclusively coordinated by oxygen donor atoms. The average Dy^{III}–O and Pr^{III}–O bond lengths are found to be 2.472 and 2.306 Å, respectively. Selected bond lengths and bond angles are listed in Table 2.

Although complexes **1** and **2** both crystallize in an orthorhombic crystal system and appear to be structurally analogous, the asymmetric unit (ASU) is distinctly different. For **2**,

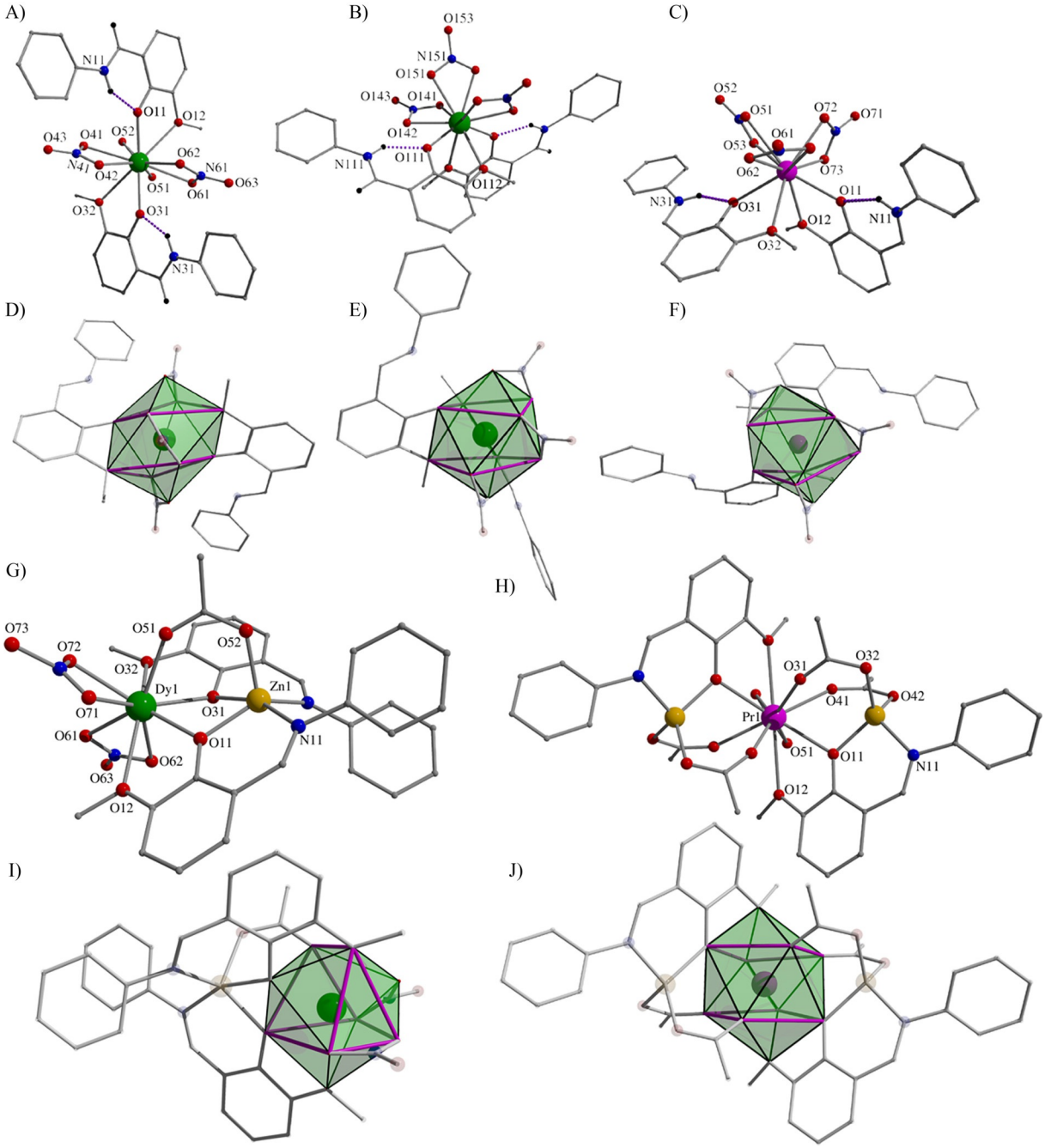

Figure 1. Ball and stick representation of crystal structure of complexes **1** (A and B), **2** (C), **3** (G) and **4** (H). D and E (for **1**), F (for **2**), I (for **3**) and J (for **4**) show the geometry around the corresponding lanthanide ions. Hydrogen atoms are omitted for clarity. The purple dotted bond represents the intramolecular hydrogen bonding in complex **1** and **2**. Color code: green = Dy, magenta = Pr, yellow = Zn, red = O, blue = N, grey = C.

there is one crystallographically distinct molecule found in the ASU. However, for **1**, in addition to one crystallographically distinct molecule, another half molecule is present. These two molecules possess the same molecular formula; however, the two molecules differ from each other by the relative orientation of ligands bound to the Dy^{III} ion. One of the molecules has three chelating nitrate ions oriented in a near trigonal planar arrangement, with the two Schiff base ligands chelating through the phenoxo and methoxy sites being perpendicular to the near trigonal plane of the nitrate ions (**1 a**, see Figure 1 A). The second unique molecule has the two HL ligands adjacent to each other, with the orientation of the chelating nitrates being distinctly different (**1 b**, see Figure 1 B). Complexes **1 a** and **1 b** are, therefore, found to be geometric isomers, crystallizing in the same crystal lattice. To the best of our knowledge, such isomerism for a lanthanide complex is observed here for the first time, although there is precedence for coordination isomers.[15] The different orientation of the nitrate ions in **1 a** and **1 b** is likely to have an influence on the magnetic properties of these complexes (see below).

Table 1. Crystallographic parameters for the complexes **1**–**4**.

	1	2	3	4
formula	$Dy_1C_{28}H_{26}N_5O_{13}$	$Pr_1C_{28}H_{26}N_5O_{13}$	$Zn_1Dy_1C_{32}H_{27}N_4O_{14}$	$Zn_2Pr_1C_{38}H_{41}N_3O_{16}Cl_4$
size [mm]	0.2×0.2×0.2	0.2×0.15×0.15	0.41×0.21×0.07	0.13×0.11×0.07
crystal system	orthorhombic	orthorhombic	triclinic	monoclinic
space group	*Aba*2	*Pbca*	$P\bar{1}$	*C*2/*c*
a [Å]	17.65(3)	9.77(6)	11.13(5)	15.58(5)
b [Å]	54.09(9)	17.24(10)	12.52(6)	15.79(5)
c [Å]	9.55(16)	36.28(2)	13.22(6)	18.94(6)
α [°]	90	90	105.88(10)	90
β [°]	90	90	91.75(5)	97.84(4)
γ [°]	90	90	94.46(6)	90
V [Å^3]	9120(3)	6111.5(6)	1764.3(14)	4620(3)
Z	12	8	2	4
ρ_{calcd} [g cm^{-1}]	1.755	1.699	1.731	1.731
2θ [°]	58.34	53.46	58.34	50
radiation	$Mo_{K\alpha}$	$Mo_{K\alpha}$	$Mo_{K\alpha}$	$Mo_{K\alpha}$
λ [Å]	0.71073	0.71073	0.71073	0.71073
T [K]	100	100	100	100
reflns	33 334	95 002	29 756	17 051
ind. reflns	11 627	6481	9054	4062
reflns with $>2\sigma(I)$	9529	5346	8566	3704
*R*1	0.0494	0.0308	0.0348	0.0630
*wR*2	0.1015	0.0639	0.0910	0.1650

In both **1** and **2**, intra- and intermolecular hydrogen-bonding interactions are found to be operative (Figure 1 and Figure S1 in the Supporting Information). The iminium zwitterions are responsible for the intramolecular hydrogen bonding (average distance NH···O = 1.8623 Å). In contrast, the nitrate ligands bound to the Ln^{III} ion facilitate intermolecular hydrogen bonding, which is clearly reflected in the packing diagram (for both **1** and **2**) shown in Figure S1. The closest Dy^{III}–Dy^{III} and Pr^{III}–Pr^{III} distances are found to be 9.189 and 9.162 Å, respectively.

In contrast to **1** and **2**, both **3** and **4** (Figure 1) are heterometallic complexes containing both lanthanide and diamagnetic Zn^{II} ions. Single-crystal X-ray diffraction reveals that **3** is a dinuclear Dy^{III}–Zn^{II} complex (Figure 1 G), which crystallizes in the triclinic space group $P\bar{1}$ (Table 1). The ASU contains the entire complex. The zinc ion displays a distorted square pyramidal geometry with a $\{N_2O_2\}$ equatorial coordination sphere derived from the two deprotonated L^- ligands. The apical position is occupied by an O atom from the acetate ligand. The trivalent dysprosium ion displays a distorted tri-capped trigonal prismatic geometry, with a $\{DyO_9\}$ coordination sphere (Figure 1 I). The linkage between the Zn^{II} and Dy^{III} ions is provided by two phenoxo bridges and a carboxylate group; the latter displays the μ-η^1-η^1 bonding mode. The methoxy group of the Schiff base ligand and the two chelating nitrate ions complete the coordination sphere of the Dy^{III} ion. Similar structures have recently been reported by several authors using other compartmentalized Schiff base ligands.[3c,16] The packing diagram of complex **3** reveals supramolecular interactions such as hydrogen bonding, which are facilitated by the nitrate ions (Figure S2 in the Supporting Information).

Single-crystal X-ray measurements reveal that **4** is a trinuclear Zn^{II}–Pr^{III}–Zn^{II} complex. In contrast to **3**, the Pr^{III} ion in **4** is sandwiched between two Zn^{II} ions, which deviate from linearity by 45° (∡Zn–Pr–Zn = 134.9(3)°). Half of the molecule is found in the ASU (one Zn^{II} and half of Pr^{III}) with the Pr^{III} ion lying on an inversion center. The Zn^{II} and Pr^{III} ions are bridged by a phenoxo oxygen atom of the deprotonated ligand and two acetate ligands both displaying a μ-η^1-η^1 coordination mode. The fourth coordination site of the Zn^{II} ion is completed by the imine nitrogen derived from the Schiff base ligand. The Zn^{II} ions display distorted tetrahedral geometries. The coordination sites of the Pr^{III} ion are completed by methoxy and nitrate groups. The Pr^{III} ion maintains a similar geometry to the Pr^{III} ion in **2**, that is, a bicapped distorted square *anti*-prism, with a $\{PrO_{10}\}$ environment (Figure 1 J). The intermolecular hydrogen bonding is effectively mediated through the nitrate and solvent molecules in the crystal lattice (Figure S2).

Static magnetic properties

Direct current magnetic susceptibility measurements were performed on polycrystalline samples of **1**–**4**, between 2–300 K in an applied magnetic field of 10 kOe. The room temperature (RT) $\chi_M T$ values for **1** and **3** are observed to be 14.06 and 14.11 cm^3 K mol^{-1}, respectively, whereas for **2** and **4**, values of 1.61 and 1.62 cm^3 K mol^{-1} are found, respectively (Figure 2).

The experimentally observed $\chi_M T$ values for **1**–**4** at RT are in excellent agreement with those expected for Dy^{III} ($^6H_{15/2}$, $g = 4/3$) and Pr^{III} ions ($^3H_4$, $g = 4/5$) of 14.17 and 1.60 cm^3 K mol^{-1}, respectively. Upon reducing the temperature, the $\chi_M T$ product decreases gradually from RT down to 60 K, for **1** and **3**. A similar situation is witnessed for complexes **2** and **4**. This observation is due to the depopulation of m_J levels of the corresponding lanthanide ion as the temperature is reduced. Below 60 K, for all four complexes, there is a drastic drop in the $\chi_M T$ value product reaching a final value of 5.13, 0.11, 4.73, and 0.31 cm^3 K mol^{-1} at 2.0 K, for **1**–**4**, respectively. The sudden drop of the $\chi_M T$ is a consequence of the magnetic anisotropy due to the intrinsic unquenched orbital angular momentum of the Dy^{III} and Pr^{III} ions. However, other factors such as intermolecular antiferromagnetic interactions and/or dipolar interactions are likely to contribute. Field-dependent magnetization measurements at 2.0 K (Figure 2 B) reveal that complexes **1** and **3** show a sudden linear increase in magnetization at low fields before deviating from linearity at higher fields, without saturation. The magnetization reaches a maximum value of 5.41 and 5.71 $N\mu_B$ at 5.0 Tesla for **1** and **3** respectively. This also suggests that both complexes possess a significant magnetic anisotropy. Moreover, this is further supported by the non-superimposable nature of the reduced magnetization curves (Figure S3 in the Supporting Information). In contrast to **1** and **3**,

Table 2. Selected bond length and bond angles for complexes **1**–**4**.

1 a	Bond length [Å]	**1 a**	Bond length [Å]
Dy(1)-O(11)	2.272(4)	Dy(1)-O(51)	2.465(5)
Dy(1)-O(31)	2.308(4)	Dy(1)-O(41)	2.495(4)
Dy(1)-O(62)	2.434(6)	Dy(1)-O(61)	2.498(5)
Dy(1)-O(52)	2.453(5)	Dy(1)-O(12)	2.702(4)
Dy(1)-O(42)	2.465(6)	Dy(1)-O(32)	2.719(4)
1 b	Bond length [Å]	**1 b**	Bond length [Å]
Dy(2)-O(111)	2.271(4)	Dy(2)-O(142)	2.527(4)
Dy(2)-O(112)	2.548(4)	Dy(2)-O(151)	2.505(4)
Dy(2)-O(141)	2.463(4)		
2	Bond length [Å]	**2**	Bond length [Å]
Pr(1)-O(11)	2.624(2)	Pr(1)-O(53)	2.607(2)
Pr(1)-O(12)	2.367(2)	Pr(1)-O(62)	2.660(2)
Pr(1)-O(31)	2.727(2)	Pr(1)-O(63)	2.532(2)
Pr(1)-O(32)	2.403(2)	Pr(1)-O(72)	2.545(2)
Pr(1)-O(51)	2.593(2)	Pr(1)-O(73)	2.545(2)
3	Bond length [Å]	**3**	Bond length [Å]
Dy(1)-O(11)	2.296(2)	Dy(1)-O(72)	2.516(3)
Dy(1)-O(31)	2.296(2)	Dy(1)-O(32)	2.561(2)
Dy(1)-O(52)	2.325(3)	Zn(2)-O(51)	1.997(2)
Dy(1)-O(62)	2.394(2)	Zn(2)-O(31)	2.516(3)
Dy(1)-O(61)	2.416(3)	Zn(2)-N(11)	2.071(3)
Dy(1)-O(71)	2.466(2)	Zn(2)-N(31)	2.096(3)
Dy(1)-O(12)	2.495(3)		
	Bond angle [°]		
Zn(1)-O(11)-Dy(1)	102.6(2)	Zn(1)-O(31)-Dy(1)	105.5(2)
4	Bond length [Å]	**4**	Bond length [Å]
Pr(1)-O(31)	2.440(4)	Zn(2)-O(32)	1.956(5)
Pr(1)-O(41)	2.460(4)	Zn(2)-O(11)	1.964(4)
Pr(1)-O(11)	2.509(4)	Zn(2)-O(42)	1.927(5)
Pr(1)-O(51)	2.622(4)	Zn(2)-N(11)	2.007(5)
Pr(1)-O(12)	2.734(4)		
	Bond angle [°]		
Zn(2)-O(11)-Pr(1)	108.07(18)		

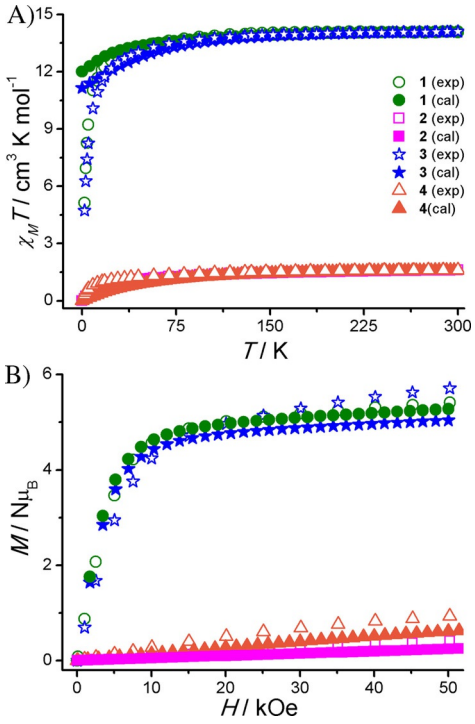

Figure 2. A) Temperature-dependent direct current $\chi_M T$ plots of complexes **1**–**4** measured at 10 kOe. B) Field dependent magnetization measurements performed on **1**–**4** at 2.0 K. The open and filled symbols in both represent the data from experiment and computed data ($\chi_M T(T)$ and $M(H)$) from ab initio calculations, respectively.

complexes **2** and **4** show a linear response over the entire magnetic field range.

Dynamic magnetic properties

To probe the magnetization relaxation dynamics of **1**–**4**, alternating current magnetic susceptibility measurements were performed between 2 and 12 K, using a 3.5 Oe oscillating magnetic field. In the absence of an applied dc magnetic field, none of the complexes display frequency-dependent out-of-phase susceptibility signals. This indicates that reversal of the magnetization orientation is extremely fast through quantum tunneling of the magnetization (QTM) due to the low-lying ground-state multiplets.

This behavior is common for Dy^{III}, Pr^{III}, and heterometallic zinc containing complexes.[3e,g,17] Upon application of an optimum bias dc magnetic field, however, both **1** (H_{dc} = 2 kOe) and **3** (H_{dc} = 3.5 kOe) reveal frequency and temperature-dependent out-of-phase susceptibility signals (Figure 3). On the other hand, no out-of-phase susceptibility signals are observed for **2** and **4** even in the presence of dc bias field (data not shown). The broad signature of the out-of-phase susceptibility signals observed for **1** (Figure 3 A) suggest that a distribution of relaxation behavior appears to be operative for this complex, whereas for **3**, it is clear that more than one magnetic relaxation pathway is operational. There could be several parameters responsible for the observation of multiple relaxation pathways in anisotropic lanthanide complexes, namely geometry assisted relaxation dynamics, for example, [Er(COT)(Cp*)] (COT^{2-} = cyclooctatetraenide, Cp* = pentamethylcyclopentadienide) and other [$Er(COT)_2$] complexes where the eclipsed and staggered conformation and/or ∡COT–Er–Cp* angle is responsible for more than one relaxation process.[18] The existence of direct and Orbach relaxation processes is witnessed in [Dy(DOTA)] complexes (H_4DOTA = 1,4,7,10-tetraazacyclododecane-1,4,7,10-tetraacetic acid).[19] Supramolecular interactions also appear to play a significant role in determining the orientation of the anisotropic axes, which in turn is correlated to its magnetization relaxation dynamics.[19b] Finally, structural disorder within the same crystal, such as Jahn–Teller isomers of a [Mn_{12}OAc] complex, resulted in the observation of multiple relaxation processes due to the different isomers having different molecular anisotropies.[20] The observation of multiple relaxation processes are more common in polynuclear anisotropic lanthanide complexes, which is a consequence of the weak super exchange interactions mediated through the bridging ligands, with the exception of few reports.[17b,21]

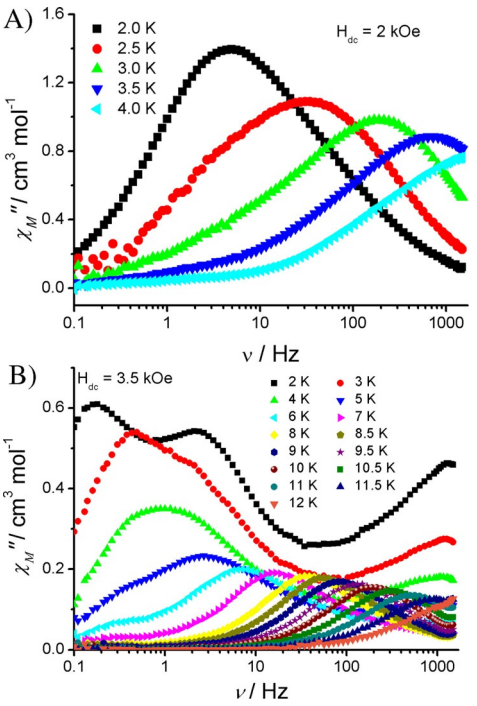

Figure 3. Frequency-dependent out-of-phase susceptibility data measured for polycrystalline sample of **1** (A) and **3** (B) at the indicated optimum dc bias field and temperatures.

The Cole–Cole plots of **1** and **3** are shown in Figure 4. Attempts to fit the Cole–Cole plot of **1** considering a single relaxation process using a generalized Debye model failed. Hence, the Cole–Cole plot of **1** was fitted using the modified Debye model given in Equation (1) (where χ_S, χ_T, ω, τ and α are adiabatic susceptibility, thermal susceptibility, frequency, relaxation time and Cole–Cole parameter, respectively) and the parameters extracted are given in Table S1 (see the Supporting Information).

$$\chi_{AC}(\omega) = \chi_{S_1} + \chi_{S_2} + \frac{\chi_{T_1} - \chi_{S_1}}{1 + (i\omega\tau_1(1-\alpha_1)} + \frac{\chi_{T_2} - \chi_{S_2}}{1 + (i\omega\tau_2)(1-\alpha_2)} \quad (1)$$

Two merged relaxation processes occur, as revealed by the Cole–Cole plot, which predicts the presence of two closely spaced relaxation phases. The α_1 value ranges from 0.002 to 0.46 and the α_2 value ranges from 0.2 to 0.36 between 3.5 and 2.0 K. The increase in both α values at low temperatures designates that the QTM process is likely to be operative at 2 K. This explains why **1** does not display any SIM behavior under a zero bias dc field. The Arrhenius plot was constructed for both these relaxation processes using the relaxation times extracted from Cole–Cole analysis and is shown in Figure 4 D. The two processes were fitted considering only the thermally activated relaxation mechanism. The effective energy barriers are found to be 16.6 cm^{-1} ($\tau_0 = 2.47\times10^{-6}$ s) and 15.8 cm^{-1} ($\tau_0 = 3.6\times10^{-7}$ s). The two different relaxation process observed for **1** are likely a consequence of the two geometrical isomers (**1a** and **1b**) present in the crystal lattice. However, to unambiguously confirm this, it is imperative to isolate a single crystal containing one of the geometric isomers only, using the HL

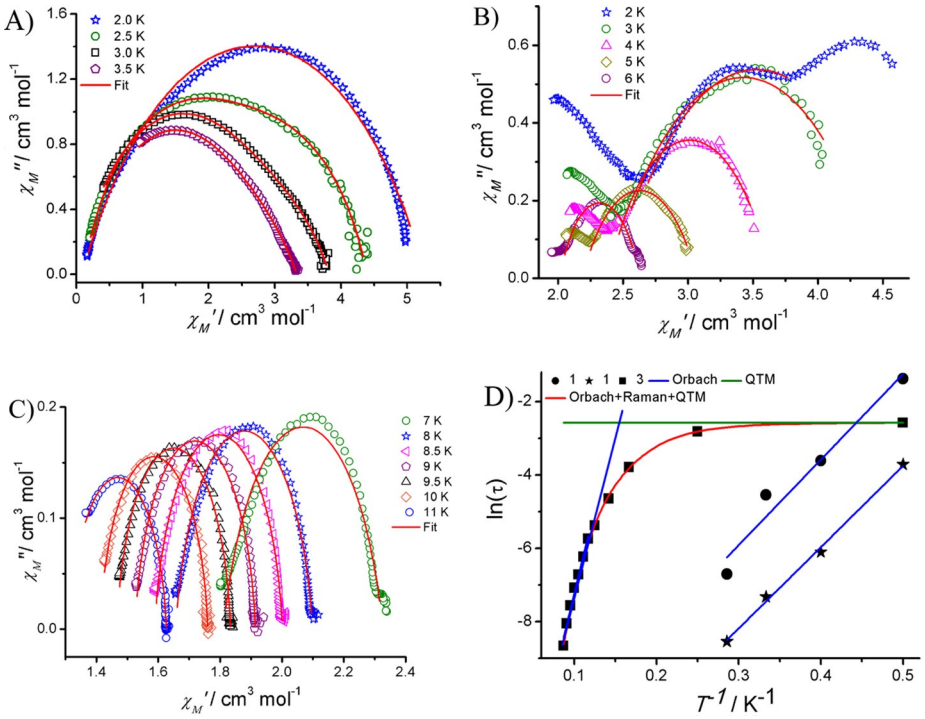

Figure 4. Cole–Cole plots of complex **1** (A) and complex **3** (B and C) measured at the indicated temperatures. The solid lines represent the best fit obtained for the parameters listed in Table S1 and S2. D) Arrhenius plots for complexes **1** and **3**; the blue line represents the linear fit with Orbach process, green represents QTM, and red represents non-linear fit including QTM, Orbach, and Raman processes (see text and [Eq. (3)] for details).

ligand (or a similar ligand) and study its behavior. This work is currently in progress.

For **3**, which consists of a single unique molecule in its ASU, the number of magnetization relaxation processes is greater than for **1** (Figure 3B and Figure 4B and C). The multiple relaxation processes are highlighted from the isothermal field dependent ac susceptibility measurements (Figure S4 in Supporting Information). At the low magnetic-field limit (<0.025 Tesla) **3** reveals a single fast relaxation process in the high frequency range. Upon increasing the magnetic field, a new slow relaxation process begins to appear in the 1–10 Hz frequency range at the expense of the fast relaxation process. Frequency-dependent ac susceptibility measurements performed at the optimum dc bias field (3.5 kOe) are shown in Figure 3B. At temperatures between 7–11 K one major relaxation is observed, which is likely to be the thermally assisted Orbach process. Upon closer inspection, the existence of a second relaxation process is also perceived at 9.5–11 K at the highest frequencies measured ($\approx$1500 Hz). Upon lowering the temperature, a third relaxation processes begins to dominate. From the Cole–Cole analysis of the relaxation data, it was not possible to fit all the relaxation processes in the temperature range 2–11 K, which might have given, distinctly, the relaxation times associated with each of the relaxation processes and their mechanism of relaxation (such as Direct, Raman, or QTM, etc.).[22] Using the ac data over the entire temperature range, it was possible to fit only the major relaxation process using a generalized Debye model [Eq. (2)] and the extracted parameters are listed in Table S2 in the Supporting Information [for a definition of the parameters, see Eq. (1)].

$$\chi_{AC}(\omega) = \chi_S + \frac{\chi_T - \chi_S}{1 + (i\omega\tau)(1-\alpha)} \quad (2)$$

The α values (0.084–0.408 for 2–11 K) are significantly smaller at higher temperature and increase gradually upon decreasing the temperature, emphasizing a distribution of relaxation times. A perfect fit could not be obtained, however, even for the major higher temperature relaxation process, which further stresses the existence of multiple relaxation phases.

Using the relaxation times extracted from the Cole–Cole plots, an Arrhenius plot was constructed for **3**, which is shown in Figure 4D. Below 6 K, a deviation from linearity was apparent, again implying that multiple relaxation processes are operational. The data over the entire temperature range were modeled by considering various relaxation processes reported in the literature[5a,23] using Equation (3).

$$\frac{1}{\tau} = \frac{1}{\tau_{QTM}} + H^2T + CT^n + \tau_0^{-1}\exp\left(\frac{-U_{eff}}{k_BT}\right) \quad (3)$$

The first term on the right hand side of Equation (3) corresponds to the relaxation process through QTM, the second term denotes the direct process, third term represents the relaxation through a Raman process, and the final term corresponds to an Orbach relaxation mechanism. To fit the Arrhenius plot of **3**, it is not necessary to use all the relaxation processes listed in Equation (3). The best fit to the data was obtained by only considering the Orbach ($U_{eff}=83\ cm^{-1}$, $\tau_0=1.36\times10^{-8}$ s), Raman ($C=0.00203\ s^{-1}K^{-3}$ and $n=5.39$), and QTM ($\tau_{QTM}=0.076$ s) processes (Figure 4D (red trace)). The parameters extracted are consistent with the other literature reports.[5a,23]

To understand the influence of the intermolecular dipolar interaction(s) on the relaxation data for **3**, an attempt was made to synthesize its diamagnetic analogue (i.e., Lu^{III}–Zn^{II} or Y^{III}–Zn^{II}) in which the paramagnetic complex would be co-crystalized within the diamagnetic matrix. Unfortunately, despite our best efforts, it was not possible to isolate the isostructural diamagnetic complex. In all cases, either a mono- or tri-nuclear zinc(II) compound was isolated (data not shown). An alternative approach was therefore sought to minimize the inter-complex dipolar interaction. Solution-based ac susceptibility measurements were performed, which are equivalent to dilution in the solid state using a diamagnetic matrix. Before carrying out such measurements, the solution stability in dichloromethane was assessed, using matrix assisted laser desorption ionization (MALDI, Figure S5) mass spectrometry. The results revealed, through a *m/z* peak at 863 (F_W of **3** is 863, which corresponds to $[ZnDy(CH_3COO)(NO_3)_2(L)_2]$, its molecular ion peak), that the solid-state structure is stable in solution (Figure S5 in the Supporting Information). The solution ac susceptibility measurement of **3** at the optimum dc bias field of 1 kOe again reveals frequency-dependent out-of-phase susceptibility signals indicative of the presence of slow magnetization relaxation. The measurement also proves that the magnetization relaxation is purely of molecular origin. The observation of broad χ_M'' signals implies that there are multiple relaxation processes, as expected (data not shown). The Cole–Cole plot constructed from solution measurements further supports the existence of multiple relaxation processes (Figure 5). Note that the existence of multiple relaxation processes for various mononuclear Dy^{III} complexes has previously been reported by several research groups.[23,24] By considering only the major relaxation process and using a generalized Debye equation [Eq. (2)], reasonable fits of the Cole–Cole data could be obtained, with α ranging between 0.48–0.89 (Figure 5 and Table S4 of Supporting Information). The very large α values indicate a significant distribution of the relaxation time. Again, relaxation times extracted from Cole–Cole data fits (shown in Figure 5) were used to construct the Arrhenius plot. The data were fitted [using Eq. (3)] by considering a thermally assisted relaxation process ($U_{eff}=89.2\ cm^{-1}$; $\tau_0=1.0447\times10^{-11}$ s), a Raman ($C=0.00611$; $n=7.1062$), and a QTM ($\tau_{QTM}=0.0768$ s) relaxation mechanism. A slightly higher thermal energy barrier is observed for the diluted sample of **3** compared to the solid-state sample. This confirms the non-negligible contribution that the dipolar interaction plays in the magnetization relaxation dynamics.

Complexes **1** and **3** can be considered magnetically as mononuclear entities (the Zn^{II} ion in **3** is diamagnetic) and due to the structural similarities the observation of a fivefold increase of the U_{eff} parameter for **3**, compared to **1** is quite surprising. Several unrelated literature reports claim that Zn^{II}-containing Dy^{III} complexes display better SIM or SMM behavior

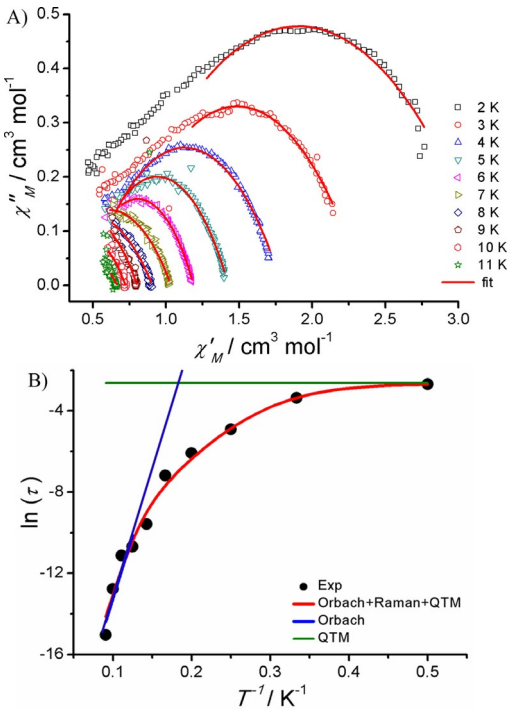

Figure 5. A) Cole–Cole plot recorded in methanolic solution of **3** in the presence of 10 kOe static magnetic field at the indicated temperatures. The solid red line represents the best fit obtained by considering a generalized Debye model using the parameters described in Table S4. B) Arrhenius plot for **3** constructed using the τ values obtained from fitting of Cole–Cole plot. The solid red line represents the best fit obtained by considering Orbach, Raman, and QTM relaxation processes.

than the parent analogue made by point-charged ligands; however, no theoretical calculations were performed in these studies to help understand the observed behavior (Table 4 and Table S3 in the Supporting Information).

Theoretical calculations

To understand the fivefold increase in the U_{eff} barrier for the complex containing the diamagnetic Zn^{II} ion, the influence that the Zn^{II} ions have on the electronic structure and therefore the magnetic anisotropy of the Ln^{III} ions was probed, using state-of-the-art ab initio calculations. Detailed post-Hartree–Fock ab initio calculations were undertaken for all complexes, **1a**, **1b**, **2**, **3**, and **4** to validate the experimental observations, using the MOLCAS 7.8[25] code, as this has proved its aptness on several occasions.[4,10,11,26] In this multi-configurational approach, relativistic effects are treated using the Douglas–Kroll Hamiltonian. For the generation of basis sets, scalar terms were included that have been used to determine the spin-free wave functions and energies through the use of the complete active space self-consistent field (CASSCF)[27] method. Spin-orbit coupling was taken into account using the RASSI-SO[28] method that uses CASSCF wave functions as the basis sets and multi-configurational wave functions as input states. The resulting wave functions and energies of the molecular multiplets were used for the calculation of the anisotropic magnetic properties and *g*-tensors of the lowest state using a specially designed routine SINGLE_ANISO.[29] As a consequence, the magnetic properties of a single magnetic ion are calculated by a fully ab initio approach, in which the spin-orbit coupling is considered non-perturbative. The atomic natural (ANO-RCC) basis set was employed for the calculation of the *g*-tensors embedded in the MOLCAS basis set library. The following contraction scheme has been employed: [8s7p5d3f2g1h] for Dy, [5s4p2d1f] for Zn, [3s2p1d] for N, [3s2p1d.] for O, [3s2p] for C, and [2s] for H during the computation of the *g*-tensors for complex **1a**, **1b**, and **3**, and [7s6p4d2f] for Pr, [5s4p2d] for Zn, [3s2p] for N, [3s2p] for O, [3s2p] for C, and [2s] for H during the computation of the *g*-tensors for complexes **2** and **4**. The ground-state atomic multiplicity of Dy^{III} is $^6H_{15/2}$, which results in eight low-lying Kramer's doublets (KD). The CASSCF calculation comprises an active space of nine active electrons in seven active orbitals (CAS(9,7)). CASSCF calculations have been performed with 21 sextets, which arise from (^{6}H, ^{6}F, and ^{6}P) multiplets. In the next step these CASSCF computed spin-free states were mixed through the RASSI module to obtain the spin-orbit states. RASSI-SO calculations were performed with 21 sextet states that arise from (^{6}H, ^{6}F, and ^{6}P) multiplets and the relative energies of the KDs were extracted. In the last step the SINGLE_ANISO code (implemented in the MOLCAS program) was used to compute the *g*-tensors. We and others have shown that 21 roots are good enough to obtain the *g*-tensors in Dy^{III} complexes,[30] thus this methodology has been employed throughout. The ground-state atomic multiplicity of Pr^{III} is $^3H_4$, which results in nine singlets for complex **2**, whereas seven singlets and one doublet are observed for **4**. For Pr^{III}, active space comprises of two active electrons in the seven active orbitals (CAS2,7). Here, we have computed 21 triplets and 28 singlets in the CI procedure, and the obtained states were later mixed into the RASSI-SO module to obtain the spin-orbit states and relative *g*-tensors. From these calculations, the static dc magnetic properties were computed, such as the magnetic susceptibility as a function of temperature and the molar magnetization as a function of magnetic field. The computed static dc properties are in excellent agreement with experimental observations, which adds confidence to the computed parameters (Figure 2 and Figures S6 and S7 in the Supporting Information). The parameters derived from the calculations can be directly taken as a tool to assess the SMM properties. For complex **1**, two different mononuclear units are present in the ASU, hence calculations are performed on both complexes labeled as **1a** and **1b**. The computed energies for the eight low-lying Kramer's doublets (KDs) span 559.7 and 455.8 cm^{-1} for **1a** and **1b**, respectively.

The computed *g*-tensors are found to be [$g_{xx}=0.020$, $g_{yy}=0.036$, $g_{zz}=19.443$] for **1a** and [$g_{xx}=0.081$, $g_{yy}=0.121$, $g_{zz}=19.092$] for **1b**, which is strongly axial for both species, but not pure Ising in nature (where $g_{xx}=g_{yy}=0$) (see Figure 6, plus Figures S8 and S9 and Tables S5 and S6 in the Supporting Information). The trend in the computed *g*-tensor of the eight lowest KDs represent typical features of low-symmetric complexes. The computed energy of the first excited Kramer's doublet, which often correlates to the height of the energy barrier (U_{eff}) in low-symmetric lanthanide single-ion magnets, is found

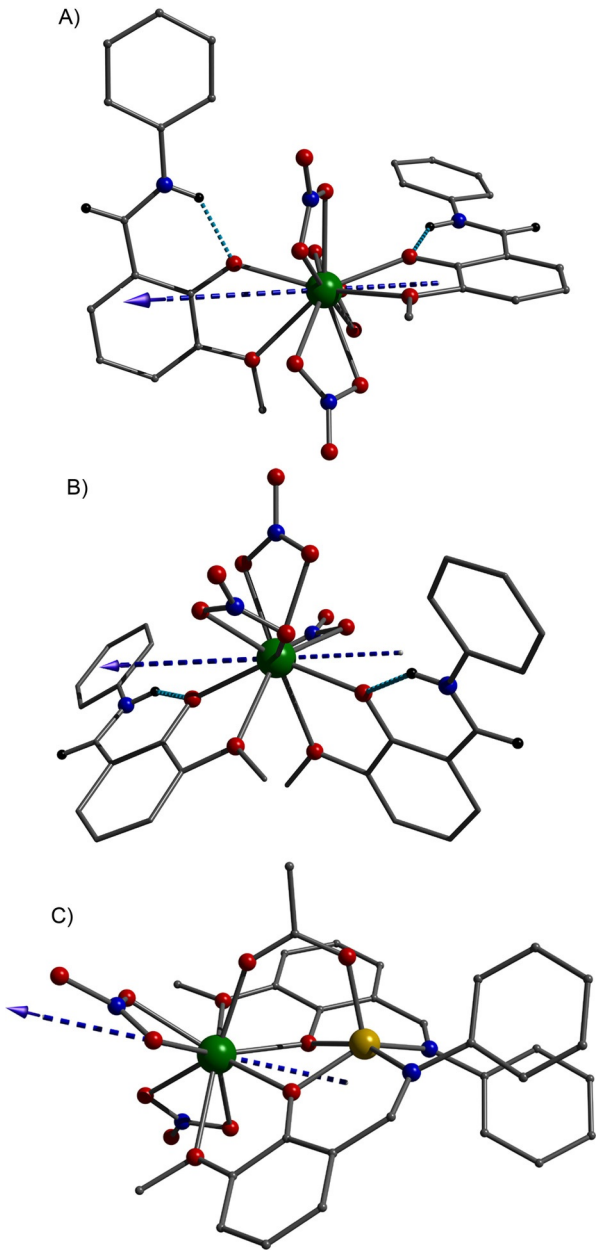

Figure 6. The molecular structure of complexes: A) **1a**, B) **1b**, and C) **3**, showing the orientation of computed easy axis anisotropy. Color code: green = Dy, yellow = Zn, red = O, blue = N, grey = C.

to be 76 and 46 cm^{-1} for **1a** and **1b**, respectively. A significant variation in the ground to first excited-state gap for **1a** and **1b** suggests that this separation is extremely sensitive to small structural changes. The computed crystal-field (CF) parameters show large and negative B_2^0 values representing the isolation of the $|\pm 15/2\rangle$ as the ground state. Wave function decomposition analysis suggests that the ground state in both cases is predominantly $m_J = |\pm 15/2\rangle$, however, the extent of mixing is significantly large; $(0.93|\pm 15/2\rangle - 0.31|\pm 11/2\rangle - 0.12|\pm 11/2\rangle)$ in **1b**, compared to $(0.96|\pm 15/2\rangle + 0.12|\pm 9/2\rangle)$ for **1a**. Thus, both the geometries are not ideally suited towards isolating a pure $|\pm 15/2\rangle$ ground state; however, complex **1a** is relatively better than complex **1b**. The SMM performance of complex **1** must therefore be considered as a combination of the properties of both complexes. It is important to note here that magnetic exchange, mediated through a dipolar interaction, is one of the key factors for diminishing the SMM characteristic in complexes such as **1** (see below).

To elucidate the mechanism of magnetic relaxation, the ab initio calculated blockade barrier was developed by computing the transversal magnetic moments between the connecting pairs (Figure 7). Due to the lack of symmetry for complex **1**, the magnetic moment between the $|\pm;1\rangle$ pair is significantly large (on the order of 10^{-2} μ_B) suggesting QTM is operative at the ground state KD (generally $10^{-5}/10^{-6}$ μ_B for complete quenching of QTM). The extent of QTM is significantly larger for complex **1b** compared to **1a**, owing to an unfavorable ligand field arrangement (see below). The QTM can best be described by the crystal-field parameters, as they are highly sensitive to the structural distortions and serve as a guide for analyzing the QTM effects. From Table 3 (see also Table S7 in the Supporting Information), it is evident that for both complexes the axial B_2^0 term is only marginally larger compared to the non-axial terms B_2^2, B_2^1, and B_4^{-1}, which implies that QTM is present due to structural distortions. The axial term in complex **1a** is relatively large compared to **1b**, representing the large QTM at the ground state of **1b**, in line with ab initio calculations. The orientation of the *g*-tensor is tilted in the direction of minimum electrostatic potential, which is found to be different for both complexes (Figure 6A and B). Thus, the difference in the magnetic properties of complexes **1a** and **1b** can be rationalized based on the number/nature of donor ligands on the axial/equatorial positions. For **1a**, three $-NO_3^-$ ligands form a distorted equatorial ligand field, whereas four O atoms occupy the axial positions. One of the O donor ligands of each L^- ligand is strongly coordinated to the Dy^{III} ion, compared to other bond lengths, indicating a significant axial ligand field offered by that particular Dy–O bond. Moreover, these O donor atoms possess the largest negative charge, thus the shorter Dy–O axial bond lengths suppress the adverse effect caused by other Dy–O bonds at the equatorial sites. This arrangement of ligands results in the stabilization of m_J $|\pm 15/2\rangle$ as the ground state. In stark contrast, complex **1b**, possesses an equatorial plane consisting of three $-NO_3^-$ ligands and one O donor atom from each $-L^-$ ligand. The two remaining O atoms of each $-L^-$ ligand are found in axial positions. Thus the Dy^{III} ion in complex **1b** faces more repulsion from the unfavorable equatorial position, leading to the stabilization of $|\pm 15/2\rangle$, however, with lower-lying excited states. The arguments presented above based on the ligand field effects are reflected in the computed ab initio blockade barrier (see Figure 7 for details).

The calculations therefore suggest significant anisotropy barriers (**1a** and **1b**); however, the presence of a substantially large QTM relaxation in the ground state is the reason behind a lack of zero-field SMM behavior for **1**. As there is a significant barrier present, ac measurements in the presence of an applied dc magnetic field allow the energies of the magnetic microstates to be perturbed, leading to a partial quenching of the tunneling mechanism and slow relaxation of the magnetization

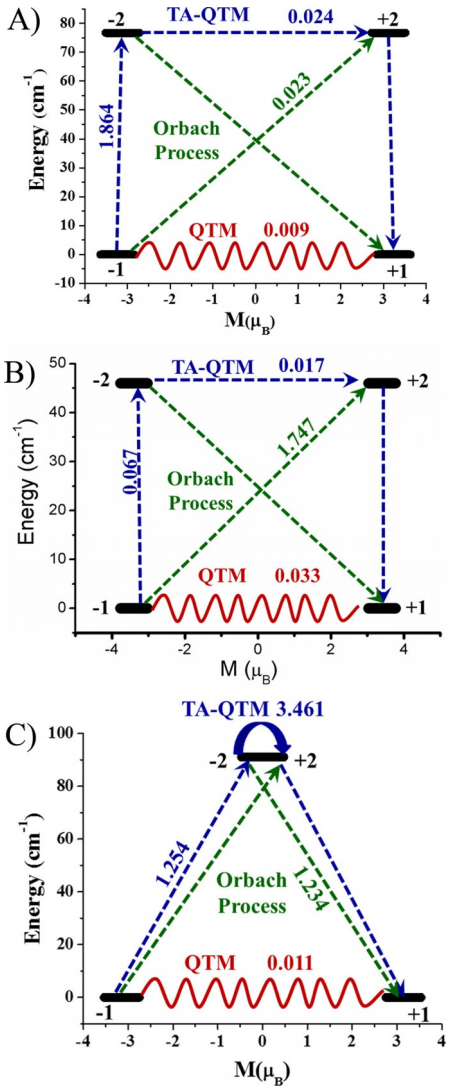

Figure 7. Ab initio computed matrix elements between the connecting pairs (ground state and first excited state) in complex **1 a** (top), **1 b** (middle), and **3** (bottom). The thick black line indicates the Kramer's doublets (KDs) as a function of magnetic moment. The dotted green lines show the possible pathway of the Orbach process. The zigzag lines connecting the ground state KDs represent the QTM. The dotted blues lines show the thermally activated-QTM through the first excited state.

Table 3. SINGLE_ANISO computed crystal-field parameters for complexes **1** and **3**.

		1 a	**1 b**	**3**
k	Q	B_k^q	B_k^q	B_k^q
2	−2	−0.633E+00	0.296E-02	**0.125E+01**
	−1	**0.194E+01**	**0.156E+01**	0.248E+00
	0	**−0.239E+01**	**−0.218E+01**	**−0.125E+01**
	1	−0.643E+00	0.109E-01	0.691E+00
	2	−0.757E+00	**0.110E+01**	−0.654E+00
4	−4	0.401E-02	−0.442E-04	**0.117E-01**
	−3	−0.430E-02	0.653E-02	**−0.288E-01**
	−2	−0.279E-02	−0.244E-04	−0.192E-02
	−1	**−0.305E-01**	−0.530E-03	−0.647E-02
	0	−0.828E-03	0.282E-03	−0.215E-03
	1	0.183E-02	−0.295E-04	−0.860E-02
	2	0.593E-02	−0.811E-02	**0.176E-01**
	3	0.842E-02	0.979E-05	**0.226E-01**
	4	0.547E-02	−0.616E-02	−0.633E-02
6	−6	−0.167E-03	−0.113E-05	−0.124E-03
	−5	−0.322E-04	**0.130E-02**	0.165E-03
	−4	0.311E-03	0.273E-05	−0.545E-05
	−3	0.255E-03	−0.918E-04	0.135E-03
	−2	−0.971E-05	0.143E-05	0.254E-03
	−1	0.227E-03	−0.247E-03	−0.609E-04
	0	0.155E-04	0.136E-04	−0.181E-04
	1	0.327E-04	0.935E-06	0.226E-03
	2	0.847E-04	0.310E-03	0.677E-05
	3	−0.450E-03	0.170E-06	0.366E-03
	4	−0.433E-04	0.329E-03	0.936E-04
	5	**0.137E-02**	−0.133E-04	0.244E-03
	6	0.766E-04	−0.546E-04	−0.324E-04

[a] The major components in the table are highlighted in bold. [b] The crystal field Hamiltonian parameter is defined as $\sum\sum_{k=-q}^{q} B_k^q \tilde{O}_{k'}^q$ where B_k^q is the crystal field parameter and $\tilde{O}_k^q$ is the extended Stevens operator. Quantization axis is chosen to be the main magnetic axes of the ground Kramer Doublet.

is observed. Despite the application of an external magnetic field, the QTM could not be completely quenched because the experimental value gives a barrier height of $\approx$16 cm^{-1} in contrast with the theoretical value of 46–76 cm^{-1}.

To understand the experimentally determined fivefold increase in the barrier height of **3** compared to **1**, and to fully understand the relaxation dynamics, CASSCF+RASSI calculations were also performed on complex **3**. The computed energy window of eight low-lying KDs for complex **3** spans a range of 396 cm^{-1}. The computed *g*-tensors for the ground state KD are found to be [g_{xx}=0.02, g_{yy}=0.04, and g_{zz}=18.82], which again reflects the presence of an Ising anisotropy that is not pure in nature (Table S8 and Figure S10 in the Supporting Information).

The ground-state magnetization axis is tilted towards one of the -NO_3^- ligands with an angle of 20.7° from the Zn–Dy molecular axis. The first excited state is 91 cm^{-1} higher in energy from the ground state, and the mismatch between the ground and excited g_{zz} orientation sets this as the U_{cal} value for magnetic relaxation. Similar to complex **1**, the computed CF parameters show large negative B_2^0 parameters, which represent the isolation of $|\pm 15/2\rangle$ as the ground state. Again, QTM is expected to be present for **3**, as a significant transverse component is found in the ground-state KD. This is in line with the experimental data, where no SMM behavior is observed in zero magnetic field (see Tables S5–S7). The U_{cal} value obtained for **3** is in close agreement with the experimental data (91 (calcd) vs. 83 cm^{-1} (exptl)). Again the mechanism of relaxation was probed using the calculated parameters. Wave function decomposition analysis suggests that the ground state is predominantly $|\pm 15/2\rangle$:−0.90$|\pm 15/2\rangle$+0.20$|\pm 9/2\rangle$+ 0.19$|\pm 11/2\rangle$ with a slight mixing from other higher excited states. This is the reason behind the presence of the non-negligible transverse anisotropy. Interestingly, the first excited KD is predominantly $|\pm 1/2\rangle$ with significant mixing from the other excited states. The computed ab initio blockade barrier reflects

a significant transition magnetic moment of 0.01 μ_B between the $|\pm;1\rangle$ pair, which clearly suggests the presence of non-negligible QTM at the ground state. The non-negligible QTM is the reason why no SMM behavior is observed at zero magnetic field. Again, as with **1**, the application of an external field lifts the degeneracy of the ground microstates, quenching QTM in the ground state and resulting in magnetic relaxation through a thermally activated process.

Next, the role of the Zn^{II} ions in increasing the U_{eff} value in this class of complex (**3** vs. **1**) was investigated. DFT calculations reveal that the bridging phenoxo oxygen atoms in **3** have larger negative charges compared to those of the coordinated oxygen atoms in **1** (−0.73 vs. −0.3, see Tables S9–S11 and Figures S11–S13). The presence of the Zn^{2+} ion leads to a larger charge polarization on the oxygen atoms, which in turn induces a large electrostatic interaction on the lanthanide ion. This eventually leads to the destabilization of excited states increasing the ground-to-first-excited state energy gap. This invariably suggests that the presence of a diamagnetic ion in the vicinity of the Ln^{III} coordination environment is likely to help to enhance the U_{eff} barrier. This polarization effect has been witnessed earlier in {Na[Dy(DOTA)]} and {Dy_4K_2} complexes.[1a,19,31]

We note that, the coordination number of Dy^{III} ion in **1** is found to be ten, whereas in **3** it is nine. It has been well established that geometry around the Dy^{III} significantly changes the relaxation dynamics behavior. Hence, a direct comparison of the computed energy barrier between **1** and **3** is not an ideal situation. To better understand whether the observed computed energy blockade difference in **1** and **3** is due to charge polarization or change in geometry around Dy^{III} (from ten to nine), ab initio calculations were performed on a Zn–Dy^{III} complex with a molecular formula of [$Zn^{II}Dy^{III}(NO_3)_3L(H_2O)$] (where H_2L = 1,3-propanediylbis(2-iminomethylene-6-methoxy-phenol), CSD reference Code: IWURAU) reported elsewhere[32] where Dy^{III} is found to be ten coordinate.

As is evident from Table S12, the ground state is axial but lacks pure Ising type with g_{xx} = 0.03, g_{yy} = 0.08, and g_{zz} = 17.87 (see Figure S14A for ground-state g_{zz} tensor alignment). The computed energies of all the low-lying Kramer's doublets in this complex span 394.7 cm^{-1}. The wave function analysis confirms the ground state to be a mixture of two different $|\pm M_J>$ states as: $0.43|\pm 15/2> + 0.43|\pm 13/2>$. The principal *g*-tensor of the first excited multiplet is tilted by 62.5° with respect to the ground state g_{zz} orientation. This outlines the computed energy barrier for the studied complex to be 98.3 cm^{-1}. This is similar to the scenario observed in **3**. Next, the mechanism for the relaxation of magnetization was elucidated (see Figure S14B). QTM within the ground state is pronounced as corroborated by a non-negligible (0.02 μ_B) matrix element pertinent to this process. The transition moment matrix element corresponding to the TA-QTM process within the first excited multiplet is significant enough (1.29 μ_B) to promote relaxation through this energy state. Additionally, the matrix element pertinent to the spin-phonon relaxation is also pronounced enough (1.55 μ_B) to further provoke relaxation through the first excited energy level.

The mechanism of relaxation analysis therefore supports a U_{cal} value of 98.35 cm^{-1}. The U_{cal} value of this Zn–Dy^{III} (Dy is ten coordinate) complex is similar to the computed barrier of **3** (91 cm^{-1}, Dy^{III} in nine coordinate) highlighting that the electronic properties are mainly influenced by charge polarization due to the Zn^{II} ion rather the coordination number in this class of complexes.

To further validate this finding, ab initio calculations were performed on Zn^{II}–Dy^{III} heterodinuclear complexes (Table 4, Figure S15) reported elsewhere[1e,3c,33,34] where the Dy^{III} ions exhibit a similar geometry as found for **3**. All these reported Zn^{II}–Dy^{III} complexes are decorated by different kinds of ligands that are distinctly different from the ligand employed here to isolate complexes **1**–**4**.

As with complex **3**, the literature reported structures maintain axiality in the ground state anisotropy, with a small transverse component. The ground state Kramer's *g*-tensor values and the energy of first excited Kramer's doublet of all these reported Zn^{II}–Dy^{III} complexes are listed in Table 4. Detailed wave function analysis and the mechanism of relaxation of these complexes are in line with the findings for complex **3**. Overall, the calculations suggest that all the reported {Zn^{II}–Dy^{III}} molecules possess more desirable SMM properties, that is, higher U_{eff} parameters, than structurally similar mononuclear Dy^{III} analogues (see Table 4 and Table S3 in the Supporting Information).

Table 4. Ab initio computed list of ZnDy complexes (coordination number of Dy is nine), which are structurally related to complex **3** (available in the Cambridge Structural Database).

No.	Molecular formula	U_{eff} [cm^{-1}] (applied field) exptl	calcd	Computed *g*-tensor g_{xx}	g_{yy}	g_{zz}	Dihedral angle (Dy-O-Zn-O) [°]	Ref.
1[a]	[Zn(μ-L)(μ-OAc)Dy(NO_3)$_2$]	–	99.96	0.03	0.05	19.11	17.91	[33]
2[b]	ZnBr(Hsal)(L)Dy(NO_3)(CH_3OH)	231, 63	193.91	0.00	0.00	19.94	6.31	[1e]
3[c]	[LZnDy(OAc)$_3$]	–	121.25	0.03	0.04	19.40	22.45	[34]
4[d]	[Zn(μ-L)(μ-9-An)Dy(NO_3)$_2$]	46.18 (0.1 T)	82.65	0.02	0.04	18.81	15.37	[3c]
5	complex **3** [ZnDy(L)$_2$(NO_3)$_2$(OAc)]	83 (0.35 T)	91.07	0.022	0.04	18.88	26.67	this work

[a] H_2L = *N*,*N*′,*N*′′-trimethyl-*N*,*N*′′-bis(2-hydroxy-3-methoxy-5-methylbenzyl)diethylenetriamine. [b] Hsal = salicylaldehyde; H_2L = 1,3-bis((3-methoxysalicylidene)amino)propane. [c] L = 1,2-bis(salicylideneaminooxy)ethane. [d] 9-An = 9-anthracenecarboxylate, H_2L as for **1**.

Although the complexes given in Table 4 are structurally similar to each other, and analogous to complex **3**, there are significant differences in the anisotropy barrier. This suggests that, apart from the charge polarization, other parameters are also likely to play a significant role in determining the computed/experimental energy barrier for the magnetization vector reversal. To understand this phenomenon, all the Zn^{II}–Dy^{III} structures were analyzed in detail. It is noticeable that the dihedral angles of the complexes listed in Table 4 are drastically different from one another. It was found that the dihedral Dy-O-Zn-O angle plays a crucial role in pushing the excited state further away from the ground state, such that a smaller dihedral angle yields a large energy barrier and vice versa. When the dihedral angle deviation is small, the Dy^{III} ion is forced into the same plane as the Zn^{II} ion and the phenoxo oxygen atoms. This scenario leads to an enhanced electrostatic repulsion, due to the presence of the additional charge density on the bridging phenoxo ligand (due to the presence of the Zn^{II} ion in the vicinity of Ln^{III}), compared to structures where the Dy^{III} ion(s) deviate from planarity (see Table 4). The extent of distortion in the dihedral angle leads to distortion around the Dy^{III} ion. Small deviations around the Dy^{III} ion geometry stabilize a large U_{eff} barrier and vice versa (Figure 8).

For the Pr^{III} containing complexes (**2** and **4**), and in contrast to **3**, the computed electronic and magnetic properties show that complex **2** lacks SIM characteristics due to the absence of bistability in the ground-state energy levels (Table S14: all the energy levels are singlet in nature). Hence, no *g*-tensors have been computed for these singlet states. Similarly, the absence of SIM behavior in complex **4** was also due to the singlet nature of the ground and the first excited energy levels, deterring us from calculating any *g*-tensor orientations and eventually preventing complex **4** from acting as a SIM (see Table S15: detection of seven singlets and one pseudo-doublet). The experimental observations of the absence of SIM characteristics in complex **2** and **4** are well reproduced in the calculations.

DFT calculations, however, reveal that the coordinated oxygen atoms in **4** also have a higher negative charge compared to that of the coordinated oxygen atom in **2** (see Tables S16–S17 and Figures S16 and S17 in the Supporting Information). The presence of the Zn^{II} ion again results in a larger charge polarization on the oxygen atom, compared to the complex where the Zn^{II} ion is absent, which in turn induces a large electrostatic interaction on the lanthanide ions. This led to the comparatively larger energy for the first excited energy state in **4** compared to **2**.

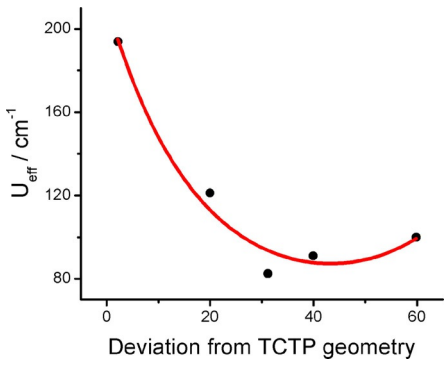

Figure 8. Plot of computed energy barrier for the complexes listed in Table 4 against the deviation from the ideal tricapped trigonal prism (TCTP) geometry calculated using continuous shape measurement software.

Conclusions

Two structurally analogous mononuclear $[Ln(HL)_2(NO_3)_3]$ (Ln = Dy (**1**) or Pr (**2**)) complexes were isolated, which were characterized by single-crystal X-ray diffraction. To detail the effect of a diamagnetic Zn^{II} ion in the vicinity of the Ln^{III} coordination sphere, two structurally similar heteronuclear complexes $[ZnDy(L)_2(NO_3)_2(CH_3CO_2)]$ (**3**) and $[Zn_2Pr(L)_2(NO_3)(CH_3CO_2)_4]$ (**4**) containing a Zn^{II} ion were isolated. The dc and ac magnetic susceptibility measurements were performed on **1**–**4** and it was revealed that complexes **1** and **3** displayed field induced single-molecule magnet behavior. For both **1** and **3** more than one magnetization relaxation pathway was observed. The anisotropy barrier extracted from the ac data reveal a fivefold increase in the anisotropic barrier for **3** compared to **1**. This has been rationalized based on detailed ab initio calculations. The reasons for such a significant increase were further corroborated through DFT calculations, which predict that the additional charge density present in the bridging phenoxo ligand (due to the presence of the Zn^{II} ion) in **3** pushes the first excited m_J level away from the ground state m_J level. The absence of the Zn^{II} ion in **1** and the distorted geometry around the Dy^{III} ion result in a smaller ground state to first excited energy gap, compared to **3**, due to the smaller charges found on the coordinated O atoms. A similar scenario is observed in complex **4** with the first excited state m_J level being significantly higher than the ground state m_J level when compared to complex **2**, where no Zn^{II} ion is present. Further detailed theoretical investigations performed on literature-reported Zn–Dy complexes that are analogous to complex **3** indeed revealed that the dihedral angle between Dy-O-Zn-O holds the key to maximizing the electrostatic repulsion between the Dy^{III} ion and the additional charge density found in phenoxo bridging ligands. The combination of excess charge density on the bridging ligand between the diamagnetic cation and paramagnetic lanthanide ion along with minimal dihedral distortion is the best combination to stabilize magnetic bistability in heteronuclear lanthanide complexes.

This study therefore reveals the unconventional method of utilizing a diamagnetic metal ion to improve the SMM behavior in any lanthanide ion complex, making it a promising route for future SMM development.

Experimental Section

Materials and methods

All reactions were performed under aerobic condition unless otherwise specified. All the chemicals and solvents of analytical grade were purchased from Alfa Aesar and used without any further purification. The Schiff base ligand was synthesized as per the litera-

ture.[14b,35] Infrared spectra were recorded for the solid samples using KBr pellets on a PerkinElmer FTIR spectrometer in the 400 to 4000 cm^{-1} range. Magnetic susceptibility measurements were performed on a Quantum Design MPMS SQUID magnetometer as described previously.[11]

X-ray crystallography

Single-crystal data were collected on a Bruker SMART Apex Duo diffractometer ($Mo_{K\alpha}$, $\lambda = 0.71073$ Å). The selected crystals were mounted on a fiber loop using Paratone-N oil and placed in the cold flow produced by an Oxford Cryo-cooling device. Complete hemispheres of data were collected by using ω and φ-scans (0.3 Å, 30 s per frame). Integrated intensities were obtained with SAINT+ and they were corrected for absorption using SADABS.[36] Structure solution and refinement was performed with the SHELX-package. The structures were solved by direct methods and completed by iterative cycles of ΔF syntheses and full-matrix least-squares refinement against F^2. It was not possible to solve the diffused electron density residual, which was associated with solvent molecules for complex **4**. This was treated with the SQUEEZE facility from PLATON, resulting in smooth convergence of all the atoms during refinement. The loop corresponding to the residual electron density (created in PLATON) is appended in the .cif file of complex **4**.

CCDC 916656 (**1**), 990256 (**2**), 990257 (**3**), and 1471848 (**4**) contain the supplementary crystallographic data for this paper. These data are provided free of charge by The Cambridge Crystallographic Dada Centre.

Synthesis of 1

The ligand HL (0.3 g, 1.3 mmol)) and $Dy(NO_3)_3{\cdot}5H_2O$ (0.2898 g, 0.6 mmol) were added to ethanol (60 mL), which resulted in an orange solution. This was then refluxed at 85–90 °C for 7–8 h. After completion of the reaction, the solution was filtered and kept for crystallization. Yellow/orange crystals were obtained upon slow evaporation of the solution at room temperature within 2–3 days. The obtained crystals, however, were found to be unsuitable for X-ray diffraction. The collected crystalline material was then recrystallized from methanol by allowing the solvent to evaporate slowly. These crystals were suitable for XRD. IR: (KBr pellet), 3424 (b,(NH)), 2942 (s,(Ar-H)), 1630 cm^{-1} (s,(C=N)). Elemental analysis: calcd: C, 41.90; H, 3.30; N, 8.70%; found: C, 41.62; H, 3.65; N, 8.77%. Yield for **1** (% based on Dy^{3+}) = 147 mg (27.7%).

Synthesis of 2

The same procedure used to isolate complex **1** was followed; however, $Pr(NO_3)_3{\cdot}6H_2O$ was used in place of $Dy(NO_3)_3{\cdot}5H_2O$. Suitable crystals for XRD were obtained from slow evaporation of the concentrated reaction mixture. IR: (KBr pellet), 3422 (b,(NH)), 2941 (s,(Ar-H)), 1632 cm^{-1} (s,(C=N)). Elemental analysis: calcd: C, 43.03; H, 3.35; N, 8.96%. Found: C, 42.92; H, 3.42; N, 8.69%. Yield for **2** (% based on Pr^{3+}) = 135 mg (26.15%).

Synthesis of 3

To a methanolic solution containing the Schiff base ligand (0.3 g, 1.3 mmol), NaOH (0.0528 g, 1.3 mmol) was added followed by the addition of $Dy(NO_3)_3{\cdot}5H_2O$ (0.2898 g, 0.065 mmol). After 15–20 minutes of stirring, $Zn(CH_3CO_2)_2{\cdot}2H_2O$ (0.29 g, 1.3 mmol) was added to this solution. Upon addition of the zinc salt the solution changed from orange to yellow. The reaction mixture was then allowed to stir for 8 hours at room temperature. The solvent was then removed under reduced pressure and the product was extracted with dichloromethane. The residue obtained after removal of the solvent was recrystallized from methanol. Suitable crystals for XRD were obtained within 2–3 days when left in the fridge at 4–5 °C. IR: (KBr pellet), 2925 (s,(Ar–H)), 1618 cm^{-1} (s,(C=N)). Elemental analysis: calcd: C, 41.70; H, 3.20; N, 6.50%. Found: C, 41.62; H, 3.15; N, 6.42%. Yield for **3** (% based on Dy^{3+}) = 160 mg (28.04%).

Synthesis of 4

The same procedure used to synthesize complex **3** was followed; however, $Pr(NO_3)_3{\cdot}6H_2O$ was used in place of $Dy(NO_3)_3{\cdot}5H_2O$. IR: (KBr pellet), 2922 (s,(Ar-H)), 1615 cm^{-1} (s,(C=N)). Elemental analysis: calcd: C, 42.29; H, 3.55; N, 4.11%. Found: C, 41.98; H, 3.42; N, 4.10%. Yield for **4** (% based on Pr^{3+}) = 172 mg (25.46%).

Acknowledgements

M.S. wishes to thank the funding agencies DST (EMR/2015/000592), DST nanomission, and IIT Bombay for financial support. G.R., K.S.M., and S.K.L. acknowledge the support of an Australia-India AISRF grant. G.R. thanks the DST-SERB (EMR/2014/00024) for funding. M.S. and G.R. thank Professor L. Chibotaru for access to the Molcas code. We thank Dr. B. Moubaraki for experimental assistance.

Conflict of interest

The authors declare no conflict of interest.

Keywords: ab initio calculations · clusters · dysprosium · magnetic properties · praseodymium · single-ion magnets

[1] a) R. J. Blagg, L. Ungur, F. Tuna, J. Speak, P. Comar, D. Collison, W. Wernsdorfer, E. J. L. McInnes, L. F. Chibotaru, R. E. P. Winpenny, *Nat. Chem.* **2013**, *5*, 673–678; b) N. F. Chilton, D. Collison, E. J. McInnes, R. E. P. Winpenny, A. Soncini, *Nat. Commun.* **2013**, *4*, 2551; c) N. F. Chilton, S. K. Langley, B. Moubaraki, A. Soncini, S. R. Batten, K. S. Murray, *Chem. Sci.* **2013**, *4*, 1719–1730; d) K. Liu, X. Zhang, X. Meng, W. Shi, P. Cheng, A. K. Powell, *Chem. Soc. Rev.* **2016**, *45*, 2423–2439; e) A. Watanabe, A. Yamashita, M. Nakano, T. Yamamura, T. Kajiwara, *Chem. Eur. J.* **2011**, *17*, 7428–7432.

[2] N. Ishikawa, M. Sugita, T. Ishikawa, S.-Y. Koshihara, Y. Kaizu, *J. Am. Chem. Soc.* **2003**, *125*, 8694–8695.

[3] a) D. Aravena, E. Ruiz, *Inorg. Chem.* **2013**, *52*, 13770–13778; b) J. Luzon, R. Sessoli, *Dalton Trans.* **2012**, *41*, 13556–13567; c) M. A. Palacios, S. Titos-Padilla, J. Ruiz, J. M. Herrera, S. J. A. Pope, E. K. Brechin, E. Colacio, *Inorg. Chem.* **2014**, *53*, 1465–1474; d) J. Ruiz, A. J. Mota, A. Rodriguez-Dieguez, S. Titos, J. M. Herrera, E. Ruiz, E. Cremades, J. P. Costes, E. Colacio, *Chem. Commun.* **2012**, *48*, 7916–7918; e) D. N. Woodruff, R. E. P. Winpenny, R. A. Layfield, *Chem. Rev.* **2013**, *113*, 5110–5148; f) X. Yi, K. Bernot, F. Pointillart, G. Poneti, G. Calvez, C. Daiguebonne, O. Guillou, R. Sessoli, *Chem. Eur. J.* **2012**, *18*, 11379–11387; g) P. Zhang, L. Zhang, S.-Y. Lin, J. Tang, *Inorg. Chem.* **2013**, *52*, 6595–6602; h) K. Bader, M. Winkler, J. van Slageren, *Chem. Commun.* **2016**, *52*, 3623–3626; i) C. J. Wedge, G. A. Timco, E. T. Spielberg, R. E. George, F. Tuna, S. Rigby, E. J. L. McInnes, R. E. P. Winpenny, S. J. Blundell, A. Ardavan, *Phys. Rev. Lett.* **2012**, *108*, 107204; j) E. M. Pineda, N. F. Chilton, R. Marx, M. Dörfel, D. O. Sells, P. Neugebauer, S.-D. Jiang, D. Collison, J. van Slageren, E. J. L. McInnes, R. E. P. Winpenny, *Nat. Commun.* **2014**, *5*, 5243; k) R. E. P. Winpenny, *Nat. Nanotechnol.* **2013**, *8*, 159–160.

[4] C. Das, S. Vaidya, T. Gupta, J. M. Frost, M. Righi, E. K. Brechin, M. Affronte, G. Rajaraman, M. Shanmugam, *Chem. Eur. J.* **2015**, *21*, 15639 – 15650.

[5] a) S. K. Gupta, T. Rajeshkumar, G. Rajaraman, R. Murugavel, *Chem. Sci.* **2016**, *7*, 5181 – 5191; b) J. Liu, Y.-C. Chen, J.-L. Liu, V. Vieru, L. Ungur, J.-H. Jia, L. F. Chibotaru, Y. Lan, W. Wernsdorfer, S. Gao, X.-M. Chen, M.-L. Tong, *J. Am. Chem. Soc.* **2016**, *138*, 5441 – 5450.

[6] Y.-S. Ding, N. F. Chilton, R. E. P. Winpenny, Y.-Z. Zheng, *Angew. Chem. Int. Ed.* **2016**, *55*, 4772 – 4776; *Angew. Chem.* **2016**, *128*, 4850 – 4854.

[7] a) J. D. Rinehart, M. Fang, W. J. Evans, J. R. Long, *J. Am. Chem. Soc.* **2011**, *133*, 14236 – 14239; b) S. Demir, I.-R. Jeon, J. R. Long, T. D. Harris, *Coord. Chem. Rev.* **2015**, *289 – 290*, 149 – 176; c) S. Demir, M. Nippe, M. I. Gonzalez, J. R. Long, *Chem. Sci.* **2014**, *5*, 4701 – 4711; d) S. Demir, J. M. Zadrozny, M. Nippe, J. R. Long, *J. Am. Chem. Soc.* **2012**, *134*, 18546 – 18549.

[8] a) N. Ahmed, C. Das, S. Vaidya, S. K. Langley, K. S. Murray, M. Shanmugam, *Chem. Eur. J.* **2014**, *20*, 14235 – 14239; b) S. K. Langley, D. P. Wielechowski, V. Vieru, N. F. Chilton, B. Moubaraki, B. F. Abrahams, L. F. Chibotaru, K. S. Murray, *Angew. Chem. Int. Ed.* **2013**, *52*, 12014 – 12019; *Angew. Chem.* **2013**, *125*, 12236 – 12241.

[9] J. D. Rinehart, J. R. Long, *Chem. Sci.* **2011**, *2*, 2078 – 2085.

[10] a) C. Das, A. Upadhyay, S. Vaidya, S. K. Singh, G. Rajaraman, M. Shanmugam, *Chem. Commun.* **2015**, *51*, 6137 – 6140; b) S. K. Singh, T. Gupta, G. Rajaraman, *Inorg. Chem.* **2014**, *53*, 10835 – 10845; c) S. K. Singh, T. Gupta, M. Shanmugam, G. Rajaraman, *Chem. Commun.* **2014**, *50*, 15513 – 15516.

[11] A. Upadhyay, S. K. Singh, C. Das, R. Mondol, S. K. Langley, K. S. Murray, G. Rajaraman, M. Shanmugam, *Chem. Commun.* **2014**, *50*, 8838 – 8841.

[12] a) D. Anvir, O. Katzenelson, S. Keinan, M. Pinsky, Y. Pinto, Y. Salomon, H. Zabrodsky Hel-Or, in *Concepts in Chemistry* (Ed.: D. H. Rouvray), Research Studies, Somerset, **1997**; b) H. Zabrodsky, S. Peleg, D. Avnir, *J. Am. Chem. Soc.* **1992**, *114*, 7843 – 7851.

[13] a) J.-P. Costes, F. Dahan, F. Nicodème, *Inorg. Chem.* **2003**, *42*, 6556 – 6563; b) W. Xie, M. J. Heeg, P. G. Wang, *Inorg. Chem.* **1999**, *38*, 2541 – 2543.

[14] a) A. Upadhyay, C. Das, M. Shanmugam, S. K. Langley, K. S. Murray, M. Shanmugam, *Eur. J. Inorg. Chem.* **2014**, 4320 – 4325; b) A. Upadhyay, S. Vaidya, V. S. Venkatasai, P. Jayapal, A. K. Srivastava, M. Shanmugam, M. Shanmugam, *Polyhedron* **2013**, *66*, 87 – 96.

[15] S. K. Langley, N. F. Chilton, L. Ungur, B. Moubaraki, L. F. Chibotaru, K. S. Murray, *Inorg. Chem.* **2012**, *51*, 11873 – 11881.

[16] a) J. P. Costes, S. Titos-Padilla, I. Oyarzabal, T. Gupta, C. Duhayon, G. Rajaraman, E. Colacio, *Chem. Eur. J.* **2015**, *21*, 15785 – 15796; b) J. Long, J. Rouquette, J.-M. Thibaud, R. A. S. Ferreira, L. D. Carlos, B. Donnadieu, V. Vieru, L. F. Chibotaru, L. Konczewicz, J. Haines, Y. Guari, J. Larionova, *Angew. Chem. Int. Ed.* **2015**, *54*, 2236 – 2240; *Angew. Chem.* **2015**, *127*, 2264 – 2268; c) I. Oyarzabal, J. Ruiz, E. Ruiz, D. Aravena, J. M. Seco, E. Colacio, *Chem. Commun.* **2015**, *51*, 12353 – 12356; d) I. Oyarzabal, J. Ruiz, J. M. Seco, M. Evangelisti, A. Camon, E. Ruiz, D. Aravena, E. Colacio, *Chem. Eur. J.* **2014**, *20*, 14262 – 14269; e) P.-Y. Shan, H.-F. Li, P. Chen, Y.-M. Tian, W.-B. Sun, P.-F. Yan, *Z. Anorg. Allg. Chem.* **2015**, *641*, 1119 – 1124; f) W.-B. Sun, P.-F. Yan, S.-D. Jiang, B.-W. Wang, Y.-Q. Zhang, H.-F. Li, P. Chen, Z.-M. Wang, S. Gao, *Chem. Sci.* **2016**, *7*, 684 – 691; g) P. L. Then, C. Takehara, Y. Kataoka, M. Nakano, T. Yamamura, T. Kajiwara, *Dalton Trans.* **2015**, *44*, 18038 – 18048.

[17] a) P.-H. Lin, I. Korobkov, T. J. Burchell, M. Murugesu, *Dalton Trans.* **2012**, *41*, 13649 – 13655; b) P. Zhang, Y.-N. Guo, J. Tang, *Coord. Chem. Rev.* **2013**, *257*, 1728 – 1763.

[18] a) K. R. Meihaus, J. R. Long, *J. Am. Chem. Soc.* **2013**, *135*, 17952 – 17957; b) S.-D. Jiang, B.-W. Wang, H.-L. Sun, Z.-M. Wang, S. Gao, *J. Am. Chem. Soc.* **2011**, *133*, 4730 – 4733.

[19] a) M.-E. Boulon, G. Cucinotta, J. Luzon, C. Degl'Innocenti, M. Perfetti, K. Bernot, G. Calvez, A. Caneschi, R. Sessoli, *Angew. Chem. Int. Ed.* **2013**, *52*, 350 – 354; *Angew. Chem.* **2013**, *125*, 368 – 372; b) G. Cucinotta, M. Perfetti, J. Luzon, M. Etienne, P.-E. Car, A. Caneschi, G. Calvez, K. Bernot, R. Sessoli, *Angew. Chem. Int. Ed.* **2012**, *51*, 1606 – 1610; *Angew. Chem.* **2012**, *124*, 1638 – 1642.

[20] a) S. M. J. Aubin, Z. Sun, H. J. Eppley, E. M. Rumberger, I. A. Guzei, K. Folting, P. K. Gantzel, A. L. Rheingold, G. Christou, D. N. Hendrickson, *Inorg. Chem.* **2001**, *40*, 2127 – 2146; b) C. Boskovic, M. Pink, J. C. Huffman, D. N. Hendrickson, G. Christou, *J. Am. Chem. Soc.* **2001**, *123*, 9914 – 9915; c) M. Soler, W. Wernsdorfer, Z. Sun, J. C. Huffman, D. N. Hendrickson, G. Christou, *Chem. Commun.* **2003**, 2672 – 2673; d) M. Soler, W. Wernsdorfer, Z. Sun, D. Ruiz, J. C. Huffman, D. N. Hendrickson, G. Christou, *Polyhedron* **2003**, *22*, 1783 – 1788.

[21] a) F. Luan, T. Liu, P. Yan, X. Zou, Y. Li, G. Li, *Inorg. Chem.* **2015**, *54*, 3485 – 3490; b) F. Luan, P. Yan, J. Zhu, T. Liu, X. Zou, G. Li, *Dalton Trans.* **2015**, *44*, 4046 – 4053; c) L. Zhang, J. Jung, P. Zhang, M. Guo, L. Zhao, J. Tang, B. Le Guennic, *Chem. Eur. J.* **2016**, *22*, 1392 – 1398.

[22] a) P.-E. Car, M. Perfetti, M. Mannini, A. Favre, A. Caneschi, R. Sessoli, *Chem. Commun.* **2011**, *47*, 3751 – 3753; b) M. Schienle, A. Kasten, P. H. Müller, *Phys Status Solidi B* **1983**, *119*, 611 – 620.

[23] E. Lucaccini, M. Briganti, M. Perfetti, L. Vendier, J.-P. Costes, F. Totti, R. Sessoli, L. Sorace, *Chem. Eur. J.* **2016**, *22*, 5552 – 5562.

[24] a) R. Marx, F. Moro, M. Doerfel, L. Ungur, M. Waters, S. D. Jiang, M. Orlita, J. Taylor, W. Frey, L. F. Chibotaru, J. van Slageren, *Chem. Sci.* **2014**, *5*, 3287 – 3293; b) Y. Rechkemmer, J. E. Fischer, R. Marx, M. Doerfel, P. Neugebauer, S. Horvath, M. Gysler, T. Brock-Nannestad, W. Frey, M. F. Reid, J. van Slageren, *J. Am. Chem. Soc.* **2015**, *137*, 13114 – 13120; c) K. S. Pedersen, J. Bendix, R. Clerac, *Chem. Commun.* **2014**, *50*, 4396 – 4415; d) K. S. Pedersen, J. Dreiser, H. Weihe, R. Sibille, H. V. Johannesen, M. A. Soerensen, B. E. Nielsen, M. Sigrist, H. Mutka, S. Rols, J. Bendix, S. Piligkos, *Inorg. Chem.* **2015**, *54*, 7600 – 7606; e) E. Lucaccini, L. Sorace, M. Perfetti, J.-P. Costes, R. Sessoli, *Chem. Commun.* **2014**, *50*, 1648 – 1651.

[25] a) F. Aquilante, L. De Vico, N. Ferré, G. Ghigo, P.-Å. Malmqvist, P. Neogrády, T. B. Pedersen, M. Pitoňák, M. Reiher, B. O. Roos, L. Serrano-Andrés, M. Urban, V. Veryazov, R. Lindh, *J. Comput. Chem.* **2010**, *31*, 224 – 247; b) G. Karlström, R. Lindh, P.-Å. Malmqvist, B. O. Roos, U. Ryde, V. Veryazov, P.-O. Widmark, M. Cossi, B. Schimmelpfennig, P. Neogrady, L. Seijo, *Comput. Mater. Sci.* **2003**, *28*, 222 – 239; c) V. Veryazov, P.-O. Widmark, L. Serrano-Andrés, R. Lindh, B. O. Roos, *Int. J. Quantum Chem.* **2004**, *100*, 626 – 635; d) J. A. Duncan, *J. Am. Chem. Soc.* **2009**, *131*, 2416.

[26] T. Gupta, G. Rajaraman, *J. Chem. Sci.* **2014**, *126*, 1569 – 1579.

[27] B. Swerts, L. F. Chibotaru, R. Lindh, L. Seijo, Z. Barandiaran, S. Clima, K. Pierloot, M. F. A. Hendrickx, *J. Chem. Theory Comput.* **2008**, *4*, 586 – 594.

[28] P. Å. Malmqvist, B. O. Roos, B. Schimmelpfennig, *Chem. Phys. Lett.* **2002**, *357*, 230 – 240.

[29] L. F. Chibotaru, L. Ungur, SINGLE_ANISO module in MOLCAS.

[30] K. Bernot, J. Luzon, L. Bogani, M. Etienne, C. Sangregorio, M. Shanmugam, A. Caneschi, R. Sessoli, D. Gatteschi, *J. Am. Chem. Soc.* **2009**, *131*, 5573 – 5579.

[31] J.-L. Liu, Y.-C. Chen, Y.-Z. Zheng, W.-Q. Lin, L. Ungur, W. Wernsdorfer, L. F. Chibotaru, M.-L. Tong, *Chem. Sci.* **2013**, *4*, 3310 – 3316.

[32] T. D. Pasatoiu, C. Tiseanu, A. M. Madalan, B. Jurca, C. Duhayon, J. P. Sutter, M. Andruh, *Inorg. Chem.* **2011**, *50*, 5879 – 5889.

[33] E. Colacio, J. Ruiz-Sanchez, F. J. White, E. K. Brechin, *Inorg. Chem.* **2011**, *50*, 7268 – 7273.

[34] S. Akine, F. Utsuno, T. Taniguchi, T. Nabeshima, *Eur. J. Inorg. Chem.* **2010**, 3143 – 3152.

[35] A. Upadhyay, N. Komatireddy, A. Ghirri, F. Tuna, S. K. Langley, A. K. Srivastava, E. C. Sanudo, B. Moubaraki, K. S. Murray, E. J. McInnes, M. Affronte, M. Shanmugam, *Dalton Trans.* **2014**, *43*, 259 – 266.

[36] SHELX-PC package **1998**, Bruker Analytical X-ray Systems, Madison, WI.

Manuscript received: January 26, 2017

Accepted Article published: February 8, 2017

Final Article published: March 23, 2017